Received: 15 January 2024 | Revised: 3 June 2024 | Accepted: 19 June 2024

DOI: 10.1002/mrm.30212

RESEARCH ARTICLE

Magnetic Resonance in Medicine

Design of calibration-free RF pulses for T_2-weighted single-slab 3D turbo-spin-echo sequences at 7T utilizing parallel transmission

Daniel Lowen[1] | **Eberhard D. Pracht**[1] | **Vincent Gras**[2] | **Aurelien Massire**[3] | **Franck Mauconduit**[2] | **Tony Stoecker**[1,4] | **Nicolas Boulant**[2]

[1]MR Physics, German Center for Neurodegenerative Diseases (DZNE), Bonn, Germany

[2]Commissariat à l'Energie Atomique, CNRS, NeuroSpin, BAOBAB, Université Paris-Saclay, Gif sur Yvette, France

[3]Diagnostic Imaging, Siemens Healthineers, Courbevoie, France

[4]Department of Physics & Astronomy, University of Bonn, Bonn, Germany

Correspondence
Tony Stoecker, German Center for Neurodegenerative Diseases (DZNE), MR Physics, Venusberg-Campus 1/99, 53127 Bonn, Germany.
Email: tony.stoecker@dzne.de

Funding information
Horizon 2020 Framework Programme, Grant/Award Number: 885876

Abstract

Purpose: T_2-weighted turbo-spin-echo (TSE) sequences are a fundamental technique in brain imaging but suffer from field inhomogeneities at ultra-high fields. Several methods have been proposed to mitigate the problem, but were limited so far to nonselective three-dimensional (3D) measurements, making short acquisitions difficult to achieve when targeting very high resolution images, or needed additional calibration procedures, thus complicating their application.

Methods: Slab-selective excitation pulses were designed for flexible placement utilizing the concept of k_T-spokes. Phase-coherent refocusing universal pulses were subsequently optimized with the Gradient Ascent Pulse Engineering algorithm and tested in vivo for improved signal homogeneity.

Results: Implemented within a 3D variable flip angle TSE sequence, these pulses led to a signal-to-noise ratio (SNR) improvement ranging from 10% to 30% compared to a two-dimensional (2D) T2w TSE sequence employing B_1^+-shimmed pulses. B_1^+ field inhomogeneities could be mitigated and artifacts from B_0 deviations reduced. The concept of universal pulses was successfully applied.

Conclusion: We present a pulse design method which provides a set of calibration-free universal pulses (UPs) for slab-selective excitation and phase-coherent refocusing in slab-selective TSE sequences.

KEYWORDS

GRAPE, kT-points, parallel transmission, spokes, ultra-high field, UPs

1 | INTRODUCTION

Turbo-spin-echo (TSE) sequences[1,2] have established themselves as indispensable tools in clinical MRI. They provide a variety of useful image contrasts for diagnosis of brain diseases such as detecting gray matter and white matter lesions in multiple sclerosis.[3,4]

These sequences are frequently employed in studies involving the hippocampus, a complex brain region of significant interest in research on neurological patholo-

gies like Alzheimer's disease, psychiatric disorders, and memory-related functions. The hippocampal formation comprises multiple subfields, which play varying roles in a multitude of psychiatric and neurological disorders.[5,6] Understanding the structural properties and alterations in these subfields provides critical insights into the nature and extent of these medical conditions.

Obtaining a precise segmentation of hippocampal subfields requires high spatial resolution (voxel size well below 1 mm^3) which is hard to achieve at a field strength of 3 Tesla or below.[7] Consequently, investigations on the hippocampus and other tiny brain structures highly benefit from increased magnetic field strengths.

Ultra-high field strengths ($\geq$ 7T) therefore can boost the signal-to-noise ratio (SNR) but introduce radiofrequency (RF) field inhomogeneities, resulting in nonuniform signal and contrast. Several strategies have been proposed to enhance the quality of whole brain T_2-weighted (T_2w) TSE-based sequences at high fields. However, these strategies either did not fully exploit pTx pulse design capabilities,[8] lacked in vivo experimental validation,[9] or were limited to nonselective three-dimensional (3D) applications.[10,11]

Slab-selective and slice-selective imaging offer the advantage of measuring axial orientations without time penalty. This is particularly interesting for nonisotropic acquisitions with high in-plane resolution, frequently employed in hippocampal imaging.[12]

Recently, the concept of UP[13] was proposed to achieve homogeneous parallel transmit (pTx) RF excitations while sparing the user a complex parallel transmission workflow consisting mainly of field map measurements and on the fly RF pulse design optimizations. Applications of UPs were investigated in various sequences[14] with pulses in the small and large tip angle regimes (excitation, inversion, and refocusing). They were introduced as k_T-point pulses and further improved with arbitrary RF and gradient shapes using the Gradient Ascent Pulse Engineering (GRAPE) approach to reduce pulse durations, decrease flip angle inhomogeneity and achieve more robustness with respect to frequency offsets.[15]

In this work, we develop a method to design universal slab-selective pulses and corresponding phase coherent refocusing pulses for usage in T_2w-TSE imaging of the brain. The way the problem is tackled provides a convenient and unique solution regardless of the position and tilt of the slab.

2 | METHODS

In our investigation, we employed a single-slab, T_2-weighted TSE sequence with a variable flip angle (vFA) train.[2,16] The sequence comprises a slab-selective excitation pulse, followed by a nonselective 180° refocusing pulse and a subsequent extended nonselective vFA refocusing pulse train.[17–19] Due to the relatively long slab-selective excitation pulse, the following 180° refocusing pulse allows diminishing the echo spacing in the subsequent echo train, as described for 3D fast spin-echo sequences by Mitsouras et al.[20] Here the RF pulse design problem therefore incorporates three distinct but entangled RF pulse types for the slab-selective TSE sequence: a 90° slab-selective excitation, a nonselective 180° refocusing pulse and a scalable nonselective refocusing pulse for the echo train (Figure 1), with phase coherence necessary to respect the Carr-Purcell-Meiboom-Gill (CPMG) condition.[21,22]

2.1 | Slab-selective excitation

Initially, we optimized a symmetric nonselective k_T-points[23] pulse to achieve uniform excitation across the entire brain. This optimization provides flexibility in selecting the actual slab position, corresponding to the imaging field of view (FOV), during the imaging session. With this approach the imaging region is not confined to a predetermined location. It is based on the assumption that if such nonselective k_T-points pulse achieves uniform

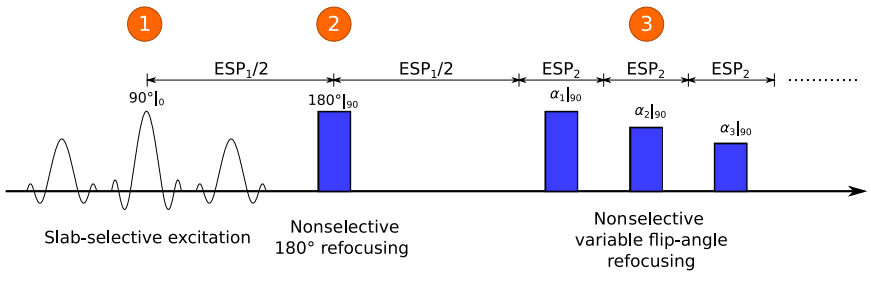

FIGURE 1 The sequence diagram illustrates the slab-selective variable flip angle turbo-spin-echo (vFA-TSE) sequence. A slab-selective k_T-spokes pulse with a target flip angle of 90° (1) is followed by a nonselective 180° refocusing pulse (2) in order to minimize the echo spacing (ESP) of the readout train (3). All radiofrequency pulses share an identical phase profile to fulfill the Carr-Purcell-Meiboom-Gill condition.

excitation across the whole brain, it will yield also a uniform excitation when the nonselective rectangular subpulses are converted into sinc-like shapes with equal areas and superposed with slab-select gradients.[24] Experimental validation supporting this assumption is provided in Figure S1.

In order to design phase coherent refocusing pulses afterwards, we conducted Bloch simulations on the returned k_T-points excitation pulse. As demonstrated in Reference 25, a symmetric pulse with a duration of T can be effectively approximated by a period of free precession during $T/2$, followed by an instantaneous excitation with a purely transverse rotation axis and another free precession of duration $T/2$. Therefore, the rotations originating from the periods of free precession can be subtracted from the rotation matrix obtained from the Bloch simulation to isolate the remaining transverse component of the rotation. The resulting orientation of the transverse rotation axis for each voxel in the brain is finally saved as the target rotation axis for the subsequent refocusing pulses. Mathematically, the resulting rotation can be described by the quaternion:

$$q = \cos(\beta/2) + \sin(\beta/2)(in_x + jn_y + kn_z), \quad (1)$$

n_x, n_y, and n_z describe the normalized vector $\hat{\boldsymbol{n}}$ defining the rotation axis:

$$\hat{\boldsymbol{n}} = (n_x, n_y, n_z) = (\sin(\theta)\cos(\phi), \sin(\theta)\sin(\phi), \cos(\theta)). \quad (2)$$

In spherical coordinates the vector is described by θ, the polar angle of the rotation axis (with respect to the static magnetic field axis) and ϕ, the azimuthal angle. β is the angle by which the magnetization is rotated around the axis defined by $\hat{\boldsymbol{n}}$. With $\theta = 90°$ a purely transverse rotation axis is achieved and therefore, ϕ defines the phase profile.

In the last step, as mentioned above, the RF and k-space coefficients of the final k_T-points excitation pulse are used to construct a slab-selective k_T-spokes pulses (Figure 2A).[26,27] For that purpose, the nonselective rectangular pulses of the k_T-points pulse are replaced by SINC-shaped pulses, incorporating the respective RF coefficients. This replacement is done in a manner that preserves the integral of the RF waveform. In the intervals between the spokes, identical gradient blips are introduced, mirroring those of the k_T-points pulse. Additionally, slab-selection gradients adjusted to the slab orientation are applied simultaneously with the subpulses.

In our study, we conducted a comparative analysis between three optimization approaches for the excitation pulse: Using a magnitude least-squares (MLS) cost function, a complex least-squares (CLS) cost function, and a combined approach (CLS+MLS).

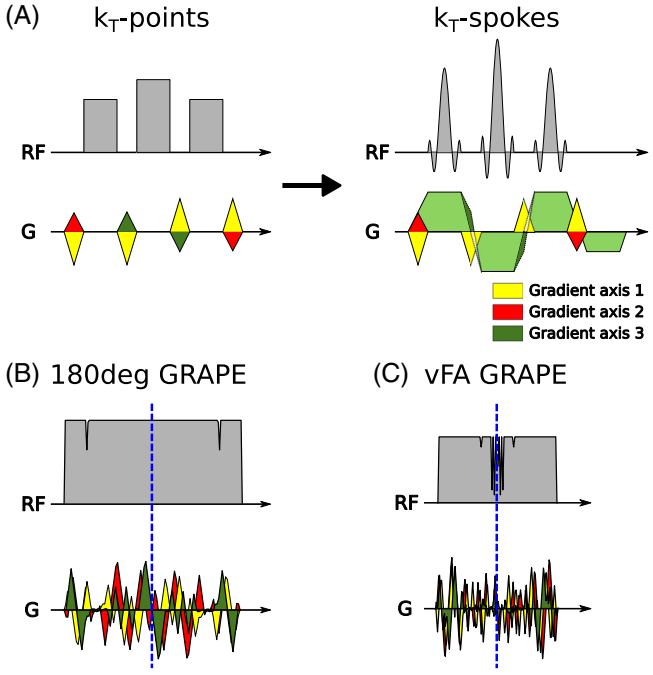

FIGURE 2 (A) The generation of k_T-spokes pulses involves transforming k_T-points pulses by substituting rectangular radiofrequency (RF)-shapes with SINC-shapes. Additionally ("spokes") gradients are applied to accomplish slab selection. (B) A symmetric 180° refocusing pulse. (C) A symmetric scalable variable flip angle (vFA) train pulse (nominal FA of 90°).

The MLS cost function is defined by

$$c_{\mathrm{MLS}} = \|\boldsymbol{w}_{\mathrm{B}_0} \cdot (\boldsymbol{\alpha}_{Bl} - \boldsymbol{\alpha}_t)\|_2, \quad (3)$$

where $\boldsymbol{\alpha}_{Bl}$ is the vector containing the flip angles of each voxel obtained from Bloch simulations and $\boldsymbol{\alpha}_t$ is the target flip angle. $\boldsymbol{w}_{\mathrm{B}_0}$ is a weighting term which improves robustness against B_0 inhomogeneities[15] and is defined by:

$$w_{\mathrm{B0},i} = 1 + \lambda|\Delta \mathrm{B}_0(\boldsymbol{r}_i)|, \quad (4)$$

where $\Delta B_0(\boldsymbol{r}_i)$ is the off-resonance at position $\boldsymbol{r}_i$ of the ith voxel and λ is a positive parameter which was set to 0.3 in this study.

Therefore, when employing the MLS cost function, the optimization focuses solely on achieving the desired flip angle, while disregarding the phase of the magnetization after excitation. This approach leads to enhanced flip angle homogeneity.[28] On the other hand, the CLS cost function with a smooth target phase distribution (e.g., where all spins end up with the same phase), has the potential to improve the optimization of phase coherent refocusing pulses, as the target phase should be easier to match in the optimization. Otherwise, because of large B_0 field offsets in some locations, for example, above the sinuses, and

a relatively long pulse duration, an MLS optimization of the slab-selective excitation pulse can yield a fast varying phase almost impossible to obtain with much shorter refocusing RF pulses. The cost function of the CLS approach is defined by

$$c_{\mathrm{CLS}} = \|\boldsymbol{w}_{\mathrm{B}_0} \cdot (\boldsymbol{q}_{Bl} - \boldsymbol{q}_t)\|_2, \tag{5}$$

where $\boldsymbol{q}_{\mathrm{B}l}$ denotes the concatenation of simulated quaternions for each voxel (periods of free precession subtracted) and $\boldsymbol{q}_t$ is the concatenation of target quaternions for each voxel. $\boldsymbol{w}_{\mathrm{B}_0}$ is a weighting term defined in Equation (4).

In the combined approach, CLS+MLS, we tried to combine the advantages of both cost functions: A slowly varying phase (which can be easier matched by the refocusing pulses) and a homogeneous flip angle distribution. For this purpose, we appended 10 iterations with the MLS cost function on the final CLS optimized excitation pulse.

2.2 | Nonselective refocusing pulses (180° and vFA)

To satisfy the CPMG condition, both the 180° refocusing and the vFA refocusing pulses must be phase coherent with the excitation pulse. To achieve this, the extracted phase of the transverse rotation axis of the slab-selective pulse serves as the target for designing phase coherent refocusing pulses (complex least-squares approach). Consequently, the target quaternion at each voxel is defined as $q_t = \cos(\alpha_t/2) + \sin(\alpha_t/2)(i\cos(\phi_{\mathrm{exc}}) + j\sin(\phi_{\mathrm{exc}}) + k \cdot 0)$ with the target flip angle α_t and the phase profile ϕ_{exc} of the excitation pulse at the respective voxel.

Additionally, following the principle proposed by Eggenschwiler et al.,[10] the refocusing pulses were designed to be symmetric in time, enabling the extraction of the effective transverse rotation axis in each iteration of the optimization process (by subtracting the periods of free precession as described in Reference 25).

Both the 180° refocusing pulse and the pulses of the refocusing train were optimized utilizing the GRAPE algorithm[15,29] to provide the maximal number of degrees of freedom to tackle the RF field inhomogeneity problem while meeting the phase constraints. The implementation of the optimization was done according to Reference 15. Since rapidly varying gradients are played out simultaneously to RF fields, we have simulated the effect of gradient delays and imperfections in Figure S2. As expected, the k_T-spokes excitation pulse is largely unaffected, while the GRAPE refocusing pulses exhibit slight deviations between ideal and real pulses. However, the mean difference in FA is approximately 1.6% for both refocusing pulses. Hence, gradient imperfections are neglected in subsequent investigations. The pulse shape of the 180° refocusing pulse is depicted in Figure 2B as an example.

The design of the scalable pulse within the refocusing train follows a similar process, employing the GRAPE algorithm and aligning its phase profile with that of the excitation pulse. Imposing symmetry not only allows to extract the effective transverse axis of the rotation, but additionally enables the scalability of the pulse to a certain degree.[25] The pulse was optimized with a target flip angle of 90° and the RF voltage constraints were set to allow a scaling of the pulse up to 135°. Figure 2C illustrates an example vFA refocusing pulse shape.

2.3 | UP design

Moreover, we explored the potential applicability of calibration-free UP[13] to the three pulses.

For that purpose, we generated one set of UP computed with a database of B_0 and B_1^+-maps acquired on 10 subjects (cf. Section 2.5). These UP were then compared to subject-tailored pulses. The universal excitation pulse was optimized with the combined CLS+MLS approach.

Given the duration of the computations necessary for GRAPE pulses (20–40 h per subject), subject tailored pulses were designed offline based on previously acquired B_0 and B_1^+ maps. These subject-specific pulses were subsequently employed in a second session involving the same subjects. The tested subjects were not included in the 10 subject database used for UP optimization. These pulses therefore could be considered "tailored" to the subject only if the head positioning within the coil was reasonably the same.

2.4 | Pulse design

All pulses were calculated using an in-house build object-oriented program written in MATLAB R2021b (The Mathworks) and the Optimization Toolbox (Version 9.2).

Figure 3 depicts the workflow to design the CLS+MLS excitation pulses and the refocusing pulses. The following notation was used:

- $\hat{\boldsymbol{x}}, \hat{\boldsymbol{y}}, \hat{\boldsymbol{z}}$ are the unit vectors in x, y, and z direction.
- $\boldsymbol{p}_{k_T}(\boldsymbol{x})$ and $\boldsymbol{p}_{\mathrm{GRAPE}}(\boldsymbol{x})$ refer to the k_T-points and GRAPE pulses represented by the respective optimization vector $\boldsymbol{x}$.
- $\boldsymbol{x} \in \mathbb{R}^{\mathrm{DOF}}$ is the optimization vector composed of the RF coefficients ($2N_{k_T} \cdot N_{TX}$ or $2N_{tp} \cdot N_{TX}$) and the gradient coefficients ($3(N_{k_T} - 1)$ or $3N_{tp}$). Each of these coefficients represents the area of a RF or a gradient block pulse.

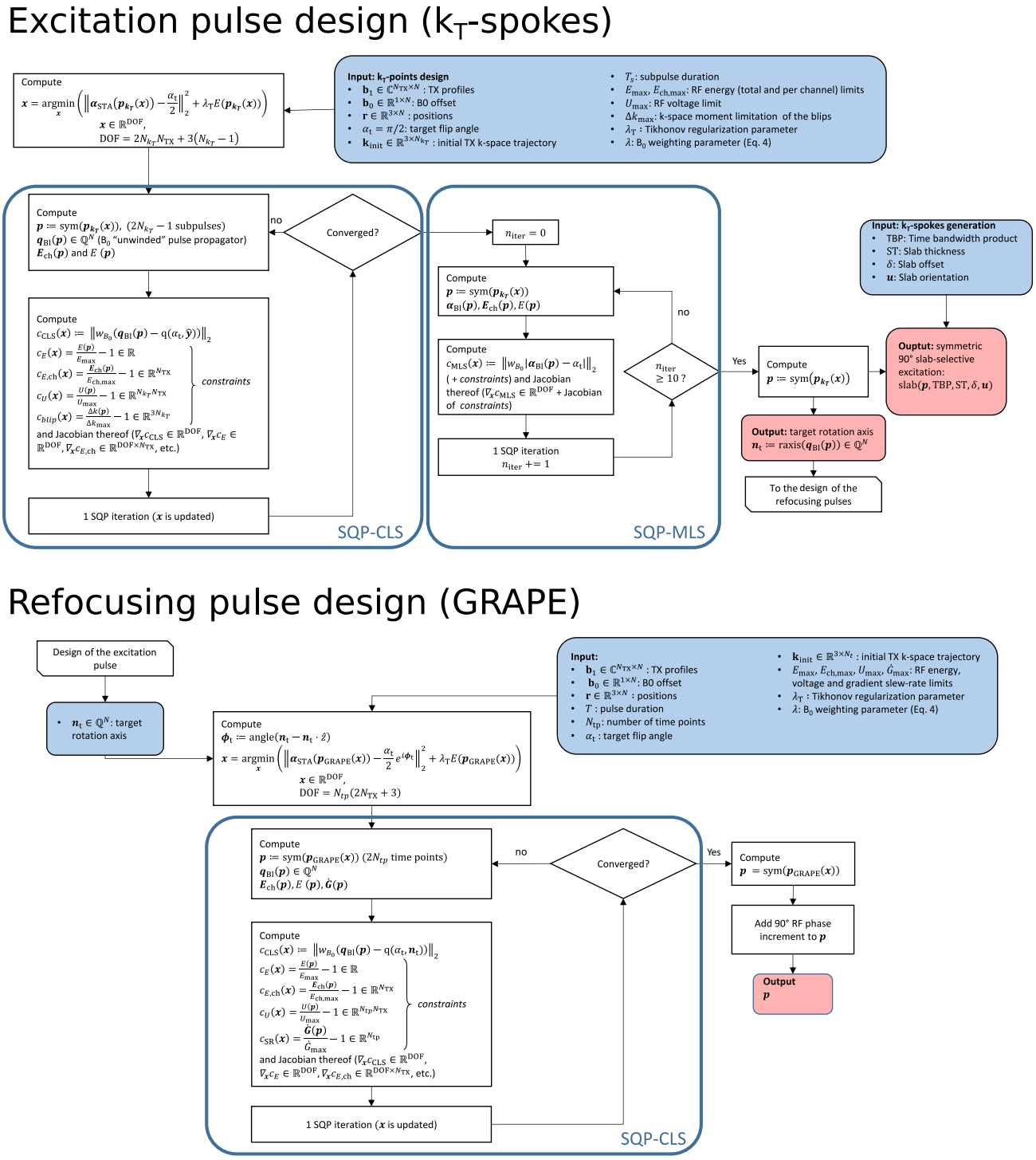

FIGURE 3 MLS+CLS pulse design flow chart for excitation k_T-spokes pulses (top) and GRAPE refocusing pulses (bottom).

- sym() describes the operator that performs the symmetric concatenation of a pulse (cf. Reference 30).
- $E()$ and $E_{ch}()$ are the total energy and the energy per channel of a pulse.
- $U()$ is the peak voltage of a pulse.
- $\Delta k()$ extracts the k-space moments of the gradient blips of a k_T-points pulse.
- $\boldsymbol{q}_{Bl}()$ is the Bloch operator extracting the quaternion rotation with "unwinding" of the B0 evolution ($\boldsymbol{q}_{\mathrm{Bl}}(\boldsymbol{p}) = \boldsymbol{q}_{fp}^{-1} \cdot \boldsymbol{q}_{\mathrm{Bl}}^{\mathrm{full}}(\boldsymbol{p}) \cdot \boldsymbol{q}_{fp}^{-1}$, where $\boldsymbol{q}_{Bl}^{\mathrm{full}}(\boldsymbol{p})$ denotes the raw Bloch propagator and $\boldsymbol{q}_{fp} = \cos(\boldsymbol{b}_0 T/4) + k\sin(\boldsymbol{b}_0 T/4)$ the free precession quaternion).
- $\boldsymbol{\alpha}_{\mathrm{STA}}()$ is the complex flip angle operator in the small tip-angle approximation.

- $\boldsymbol{\alpha}_{Bl}()$ is the flip angle operator derived from the Bloch propagator.
- $q(\alpha, \boldsymbol{n})$ is the quaternion representing a rotation of angle α around the axis $\boldsymbol{n}$.
- slab() is the operator that transforms the (nonselective) k_T-points pulse into a k_T-spokes pulse.
- raxis() extracts the rotation axis of a quaternion.

The (k_T-points) excitation pulse was initialized with 100 different random k-space trajectories and RF coefficients obtained by solving the linear optimization problem of the spatial domain method (in the small tip angle regime)[31] with a zero phase target and Tikhonov regularization ($\lambda_T = 6000$) in order to ensure that all constraints (peak RF amplitude and RF energy) were satisfied. The result yielding the lowest Flip-Angle Normalized Root Mean Square Error (NRMSE) was selected.

Following the previous initialization, RF and k-space trajectories were optimized simultaneously[32] using sequential quadratic programming[33] available in the MATLAB function fmincon, considering explicit RF power and maximum gradient amplitude and slew rate constraints. This variant of the active-set program is somewhat slower[33] but was found to be more accurate and more stable in the enforcement of the constraints. For the excitation pulse, we constrained the maximal blip moment to adhere to slew rate limitations, even after incorporating trapezoidal gradients for slice selection with the thinnest slab thickness intended for use.

In this study, we employed excitation pulses comprising nine subpulses (corresponding to $[N_{k_T} = 5]$ in our workflow) with a subpulse duration of $T_s = 0.8$ ms and a gradient polarity switching time of 0.2 ms, leading to a total pulse duration of 9.5 ms. A lower number of subpulses would require longer subpulse durations and lead to severe dropouts at regions with high B_0 deviations. The SINC-shaped profiles of the final spokes pulse had a time bandwidth product of 5. This value was chosen as high as possible, to provide a uniform slab profile, while simultaneously minimizing the subpulse durations to enhance the homogeneity in regions with high B_0 deviations and maintaining peak power within hardware constraints.

Likewise, the duration of the refocusing pulses was chosen as short as possible. Various durations have been tried and pulses with the lowest final cost-function value were selected. The 180° refocusing pulse resulted in a duration of 1.5 ms and the refocusing train pulse was set to be 1 ms. The constraints of the refocusing train pulses were chosen to permit a scaling of the pulse up to 135°.

In all cases, constraints were established to adhere to hardware limitations, including a maximal gradient field strength of 70 mT/m, a gradient slew rate of 200 T/m/s, a peak voltage of 190 V, a total power of 8 W, and a power per transmit channel of 1 W. While SAR limitations were not explicitly integrated into the pulse design process, they were considered during subsequent scaling of the flip angle train, as described in the Reference 19.

2.5 | Experiments

Experiments were conducted on a MAGNETOM 7T Plus scanner (Siemens Healthineers) using a head array coil with 32 receive and eight transmit channels (Nova Medical). In vivo experiments were performed in accordance with guidelines set by the institutional review board.

In a first session, we acquired B_0-maps with a 3D multiple gradient recalled echo (GRE)[34] on 12 healthy human subjects. Additionally, to reconstruct the complex sensitivity profiles of all eight channels of the head array coil, B_1^+-maps of each channel were acquired by using the actual flip-angle imaging sequence (AFI).[35]

To assess the efficacy of the three design approaches (MLS, CLS, and CLS+MLS) of the excitation pulse, we compared their FA-NRMSE (obtained retrospectively from Bloch simulations) and the normalized gray matter signal of the central echo (using Extended Phase Graph (EPG)[36,37] simulations based on B_0 and B_1^+ maps acquired in the second imaging session of the two subjects.) Subsequently, we conducted actual 3D slab-selective TSE scans using the same pulses to verify the findings experimentally. On these scans the SNR divided by the square root of the acquisition time was evaluated utilizing the so-called difference method.[38]

Additionally, we conducted EPG simulations and *in vivo* scans for SNR comparison with sets of subject tailored and UP.

Finally, we compared the slab-selective vFA TSE sequence employing UPs to a vendor provided 2D T_2w TSE sequence. The pulses used in the 2D T_2w TSE sequence were B_1^+-shimmed (employing the vendor provided implementation and protocol) to their respective FOV. Two healthy subjects were scanned with a high resolution protocol ($0.4 \times 0.4 \times 1.0\,\text{mm}^3$) and the resulting image SNR divided by the square root of the respective acquisition time was compared. Furthermore, we compared both approaches in terms of the contrast to feature ratio (CFR) between gray matter (GM) and white matter (WM), the coefficient of joint variation (CJV), and the width of the point-spread-function. The CFR is defined as $(I_{WM} - I_{GM})/(I_{WM} + I_{GM})$ where I_{WM} is the average signal intensity of white matter and I_{GM} is the average signal intensity of gray matter. We chose the CFR over the CNR as it better describes the visual perception of the human eye. CJV was proposed as a metric to asses intensity nonuniformity

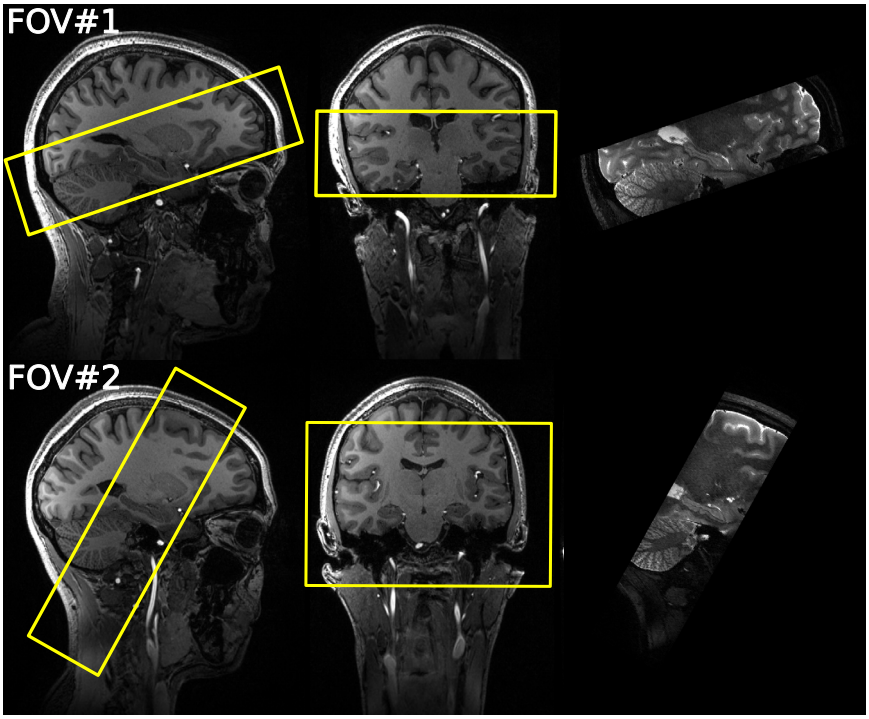

FIGURE 4 The slab-selective turbo-spin-echo (TSE) is acquired in two orientations. FOV#1 covers the frontal lobe, the temporal lobes and most of the cerebellum. FOV#2 is oriented perpendicular to the long axis of the hippocampus. At the right side the acquired slab in sagittal orientation is illustrated.

by Ganzetti et al.[39] and is defined as $(\sigma_{WM} + \sigma_{GM})/(I_{WM} - I_{GM})$, where σ_i is the SD of the respective tissue class i. Finally, the full width at half maximum (FWHM) of the point-spread-function was extracted from the images using 3dFWHMx from the AFNI toolkit.[40,41]

In an exemplary hippocampal imaging setup, one subject was scanned, with the FOV adjusted perpendicular to the long axis of the hippocampus.

A low resolution protocol was chosen for RF pulse comparisons. Sequence parameters were: TR/TE (TEeffective) = 4000/240 (98) ms, Echo spacing = 4.17 ms, 1.4 averages, 36 slices per slab, 33.3% slice oversampling, R_{PI}=1x3z1 (CAIPIRINHA[42]), readout pixel bandwidth = 485 Hz, turbo factor = 107, voxel size = $1.0 \times 1.0 \times 1.5\,mm^3$, FOV = $224 \times 180 \times 54\,mm^3$, TA = 2:08 min.

For comparison to a 2D T_2w TSE sequence a high-resolution protocol was selected for the slab-selective TSE, as it is used in typical hippocampus measurements, with following parameters: TR/TE (TEeffective)=4000/281 (105) ms, Echo spacing = 4.87 ms, 1.4 averages, 56 slices per slab, 28.6% slice oversampling, R_{PI}=1x3z1 (CAIPIRINHA), readout pixel bandwidth = 488 Hz, turbo factor = 107, voxel size = $0.4 \times 0.4 \times 1.0\,mm^3$, FOV = $224 \times 182 \times 56\,mm^3$, TA = 7:00 min.

The corresponding multislice 2D T_2w TSE was acquired utilizing B_1^+-shimming with: TR/TE = 8090/76 ms, Echo spacing = 15.3 ms, 1 average, 55 slices, readout pixel bandwidth = 155 Hz, turbo factor = 9, voxel size = $0.4 \times 0.4 \times 1.0\,mm^3$, FOV = $224 \times 182 \times 55\,mm^3$, TA = 6:30 min.

The FOV was determined based on the following considerations: It included the cerebellum due to the lowest values of B_1^+ with conventional circular polarized pulses in that region. Furthermore, the FOV covered the inferior part of the frontal lobe and the temporal lobes because the neighboring air cavities in these regions induce significant B_0 inhomogeneities. Consequently, an oblique slab orientation was selected, as depicted in Figure 4 (FOV#1). The B_0 shim volume was set to cover the entire brain, consistent with the shim volume utilized to acquire the underlying B_0 maps.

Additionally, images were acquired in a different orientation (FOV#2 in Figure 4) employing the slab-selective and a 2D TSE to facilitate a comparison in an exemplary hippocampus imaging setup. The FOV orientation provides high in-plane resolution perpendicular to the long axis of the hippocampus, which is best suited for hippocampal subfield segmentation.[12] The shorter axis of the FOV (80% FOV phase) was consistently oriented in the right-left direction of the patient in all cases.

3 | RESULTS

FA-NRMSE values, simulated signal, and measured SNR values of all conducted experiments and simulations comparing various pulses employed in the slab-selective TSE are summarized in Table 1.

Figure 5 provides the comparison between the three approaches for designing the excitation pulse. Additional

TABLE 1 Comparison of results from a slab-selective TSE sequence utilizing different pulse designs.

	FA-NRMSE (%)		Simulated signal (a.u.)		SNR	
	Subject 1	**Subject 2**	**Subject 1**	**Subject 2**	**Subject 1**	**Subject 2**
CP	37.1	35.8	7.2	7.5	1.49	1.90
CLS	20.8	29.4	12.7	11.8	2.29	1.74
MLS	**10.8**	**9.9**	12.9	12.8	2.01	1.61
CLS+MLS	13.0	14.0	**13.1**	**13.0**	**2.64**	1.84
UP	14.0	14.9	12.9	12.9	2.04	**1.91**

Note: Circularly polarized (CP), various subject tailored, and UP were employed. Subject tailored pulses were optimized either with a CLS (complex least-squares), a MLS (magnitude least-squares) cost function or a combined approach (CLS+MLS). Universal pulses (UP) were designed with a CLS+MLS approach. The FA-NRMSE results from Bloch simulations, the mean signal of the central echo from EPG simulations and the measured signal-to-noise ratio (SNR) divided by the square root of the acquisition time are displayed. Bold numbers indicate the best value for each column.

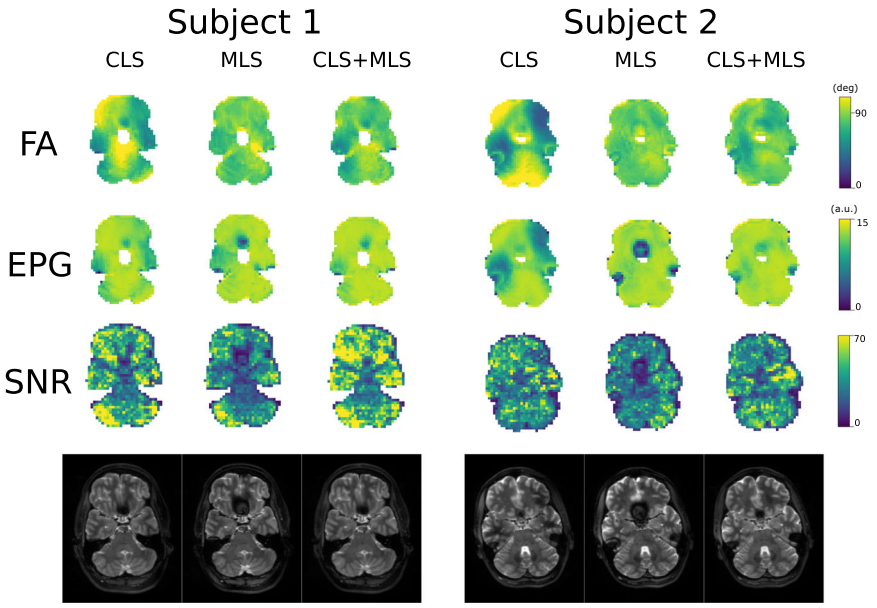

FIGURE 5 CLS versus MLS versus CLS+MLS excitation: Comparison of simulated excitation flip angle (FA), normalized gray matter signal of the central echo in an EPG simulation (EPG), measured signal-to-noise ratio (SNR), and anatomical images for an experiment using excitation pulses designed with a CLS cost function, a MLS cost function and a combined approach of CLS and MLS (CLS+MLS).

slices of the in vivo measurements and results from CP mode pulses are presented in Figure S3 for subject 1 and in Figure S4 for subject 2. The corresponding values are displayed in the rows CP, CLS, MLS, and CLS+MLS in Table 1. A notable improvement is evident across all designed pulses with respect to the CP mode pulses. As expected, the MLS optimization yields the most uniform FA distribution throughout the brain, with an improvement of approximately 50%–65% in FA-NRMSE compared to the CLS approach. With just 10 additional iterations using the MLS cost function, initialized with the CLS excitation pulse, the FA-NRMSE of the CLS+MLS pulse could be significantly enhanced by around 35%–50%, nearly reaching the uniformity of the MLS pulses. Likewise, the EPG simulation of the MLS pulse results in a higher average signal compared to the CLS pulse, but the CLS+MLS approach achieves superior outcomes. On the other hand, MLS pulses exhibit pronounced signal dropouts in regions adjacent to the sinuses with high B_0 deviations (such as the temporal lobes and lower part of the frontal lobe), whereas CLS pulses alleviate this effect. These imperfections are not reflected in the FA maps and originate from a lack of phase coherence between the excitation and the refocusing pulses. In the anatomical images, these imperfections lead to dark spots and a dramatic loss of contrast. As intended, the CLS+MLS approach combines the benefits of homogeneous FA throughout the brain with enhanced phase coherency in regions with high B_0 offsets.

Subject tailored pulses demonstrate superior performance compared to UP with regard to FA-NRMSE and simulated signal (cf. Figure 6). Rows CLS+MLS and UP in Table 1 illustrate the respective quantitative performances of subject tailored or UP with the same pulse design approach. While SNR decreased in subject 1, it increased in subject 2 with UP. However, signal dropouts caused by B_0 off-resonances are less pronounced with UP in compared

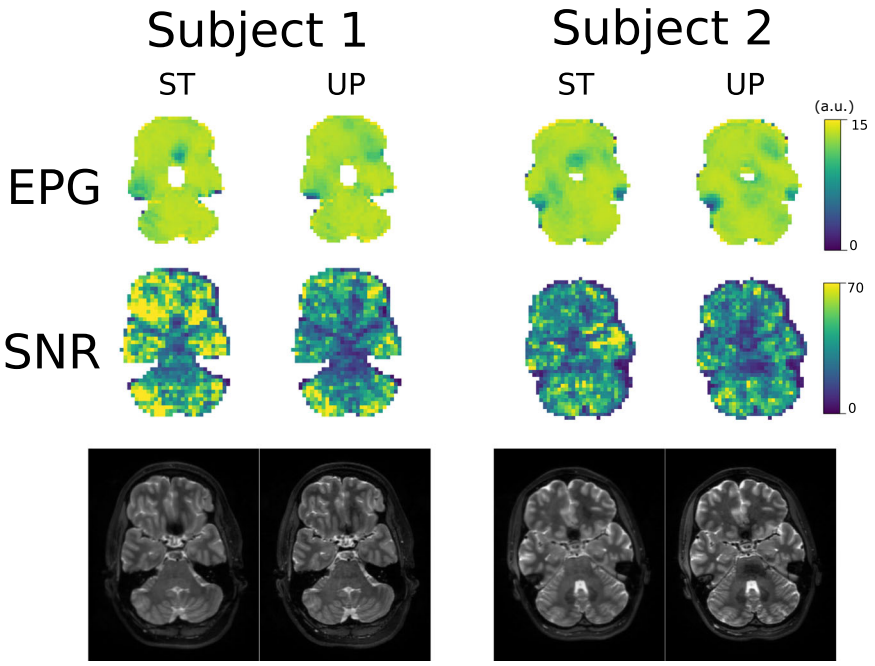

FIGURE 6 Tailored versus UP: Comparison of simulated signal (EPG) and SNR maps, along with anatomical images for the slab-selective TSE sequence employing subject tailored pulses (ST) or universal pulses (UP). In both cases a CLS+MLS approach was used.

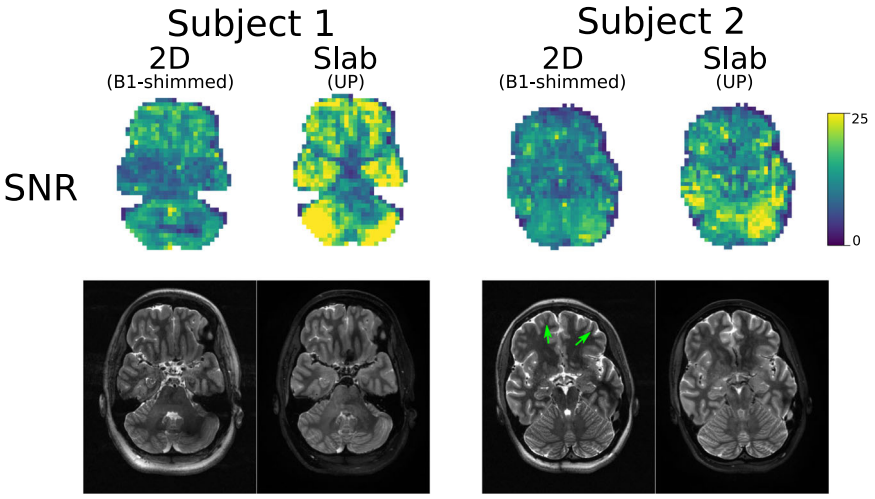

FIGURE 7 Signal-to-noise ratio (SNR) maps and anatomical images are compared for a two-dimensional (2D) T_2w turbo-spin-echo (TSE) sequence with B_1^+-shimming (2D) and the slab-selective TSE sequence employing universal pulses (Slab) with high resolution protocols. Green arrows indicate motion artifacts.

to subject tailored pulses (also cf. Figure S5 for additional slices).

In the final comparison, Figure 7 illustrates the slab-selective vFA TSE with UP alongside a B_1^+-shimmed 2D T_2w TSE sequence with high-resolution protocols (see also Figure S6 for more slices). SNR values divided by the square root of the acquisition time ("imaging efficiency"), CFR, CJV, and FWHM values are presented in Table 2. Both techniques produced a similar SAR deposition. However, a CP mode 2D TSE would only lead to a SAR load of 35%, B_1^+-shimming increased the power deposition to 88% of the SAR limit. Similarly, the slab-selective TSE resulted in 91% of SAR.

Advantages of the 2D TSE include the sharper point-spread-function, resulting in less blurry images and more robustness to B_0 inhomogeneities. Nevertheless, signal loss is also observed for 2D TSE acquisitions in the temporal lobes due to B_0 deviations. In contrast, the slab-selective TSE exhibits improved SNR, especially in the cerebellum and the temporal lobes, and provides a similar CFR. An analysis of the SNR with respect to the voxel position within the FOV is plotted in Figure S7, where no significant signal reduction due to the imperfect slab profile is visible. Regarding CJV, the slab-selective TSE shows substantially more homogeneous signal for GM and WM. Moreover, the 2D TSE turned out to be more sensitive to motion and had to be repeated for the first subject, as even small motions lead to severe motion artifacts. Slight artifacts still remained and are indicated by green arrows in Figure 7.

TABLE 2 Comparison of results from a two-dimensional (2D) T_2w turbo-spin-echo (TSE) sequence with B_1^+-shimming (2D) and a slab-selective TSE sequence utilizing universal pulses (Slab).

	SNR		CFR		CJV		FWHM	
	Subject 1	**Subject 2**	**Subject 1**	**Subject 2**	**Subject 1**	**Subject 2**	**Subject 1**	**Subject 2**
2D (B1-shimmed)	0.52	0.45	0.218	**0.260**	230	745	**2.83**	**2.81**
Slab (UP)	**0.66**	**0.50**	**0.233**	0.238	**32**	**49**	3.41	3.41

Note: The measured signal-to-noise ratio (SNR) divided by the square root of the acquisition time, the contrast to feature ratio (CFR), the coefficient of joint variation (CJV) and the full width at half maximum (FWHM) of the point-spread-function are displayed. Bold numbers indicate the best value for each column.

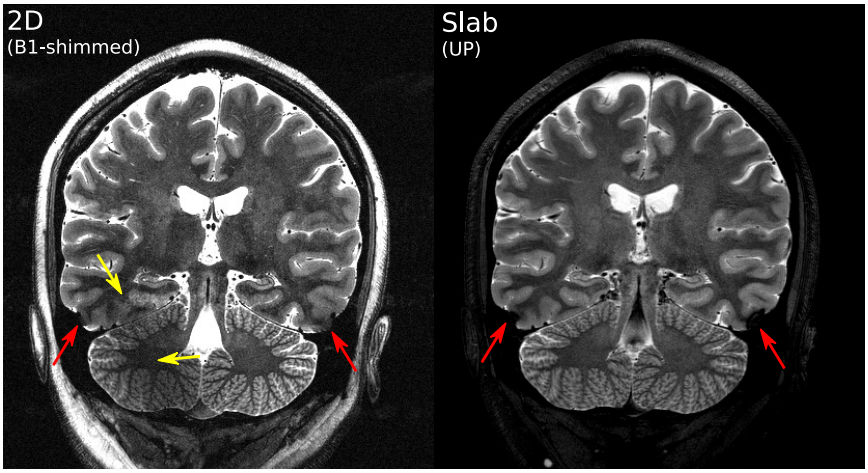

FIGURE 8 Comparison of T_2-weighted acquisitions ($0.4 \times 0.4 \times 1\,mm^3$ with FOV#2) using a typical hippocampus imaging protocol: (A) two-dimensional turbo-spin-echo (2D TSE) with B_1^+-shimming and (B) slab-selective variable flip angle (vFA) TSE with universal pulses (UPs). The 2D TSE exhibits signal and contrast deterioration in the cerebellum and the temporal lobe above (yellow arrows). The slab-selective TSE shows signal loss in the temporal lobes induced by B_0 deviations (red arrows). This effect is less severe in 2D TSE.

Additionally, one subject was scanned with the acquisition plane perpendicular to the long axis of the hippocampus (Figure 8). Darkened areas in the cerebellum and temporal lobes are clearly visible, as indicated by the yellow arrows. The reduced signal leads to decreased contrast and makes GM and WM indistinguishable in some parts of the temporal lobes. However, local B_0 deviations can still corrupt the slab-selective TSE image of the temporal lobes more strongly compared to the 2D TSE (red arrows). Furthermore, the fat signal in the slab-selective TSE image is significantly reduced. Bloch simulations at fat frequency (shifted by 3.5 ppm) show a flip angle reduction of approximately 80% for all three UP. Consequently, fat signal is nearly absent.

4 | DISCUSSION

In this study, we have demonstrated a substantial enhancement of slab-selective TSE at ultra-high fields through the utilization of dedicated pTx pulses enabled by a new pulse design strategy. We successfully generated homogeneous nonselective k_T-points pulses for the entire brain and subsequently transformed them into slab-selective k_T-spokes pulses for slab-selection. Corresponding nonselective refocusing pulses were optimized to satisfy the CPMG condition and ensure homogeneous signal throughout the entire slab. We created a set of three phase-coherent pulses and compared different pulse design approaches.

Each cost function (CLS or MLS) used to design the excitation pulse offers distinct advantages. Intuitively, a MLS approach makes sense because the GRAPE refocusing pulses have more degrees of freedom to match the phase profile of the excitation pulse. Therefore, a MLS cost function eases the pulse design problem and leads to more homogeneous FA distributions, resulting in more uniform signal across large parts of the brain. However, the long duration of the excitation pulse (9.5 ms) inherently leads to a rapidly changing phase of the effective transverse axis of rotation in regions with pronounced B_0 field strength deviations. But the MLS cost function does not take that into account. With the refocusing pulses being considerably shorter, achieving an exact match for this intricate phase profile becomes challenging, even with the incorporation of numerous degrees of freedom through the GRAPE algorithm. The CLS approach, on the other hand, better supports the design of consecutive refocusing pulses, as it aims at achieving a more homogeneous phase also in regions with high B_0 deviations, thereby promoting phase coherence more easily with the refocusing pulses. Yet this comes at the cost of less homogeneous flip angles, but regains signal in areas next to air cavities, namely the

lower part of the frontal lobe and temporal lobes. Averaged over the entire imaged slab, CLS excitation pulses achieved higher signal intensities, but less homogeneous contrast. Therefore, we decided to combine the CLS and MLS approach. A completely uniform phase profile (as it is targeted with our CLS cost function) is not required and a slowly varying phase relaxes the pulse design problem, leading to improved FA distributions. Consequently, optimizing the final CLS pulse with the MLS cost function for only 10 iterations prevents rapid phase changes but improves the achieved FA considerably. The strategy therefore can possibly be revised with a more elaborate regulation for smooth phase profiles. Nevertheless, it was possible to increase the final SNR substantially and remain more robust to static field variations with the CLS+MLS approach. For this reason, it was chosen as the preferred method for designing UP.

Additionally, we conducted a comparative assessment of the performance between subject-tailored (up to small differences in head position) and UP. The results demonstrated that UP not only enhance flip angle homogeneity across different subjects[13] but also maintain phase coherence between pulses across all subjects. As anticipated, UP achieved worse FA homogeneity across both subjects and lower SNR compared to subject tailored pulses in one subject, but yielded higher SNR values for subject 2. Signal attenuation near the brain stem was evident with UP, while B_0 artifacts even improved in subject 1. The overall enhanced SNR in subject 2 may be attributed to the calculation of subject-specific pulses based on B_0 and B_1^+ maps acquired in a separate session. Consequently, variations in head orientation and the B_0 shim during the measurement session could lead to suboptimal performance of those subject-"tailored" pulses. In contrast, UP are less sensitive to differing shims and head orientations, as they incorporate maps from various subjects with distinct head shapes and positions. Another drawback of subject tailored pulses is that their usage necessitates to acquire B_0 and B_1^+ maps of each measured subject in a separate session, as GRAPE pulse calculations are very time-consuming. Even rapid mapping techniques and pulse calculations, as demonstrated in previous studies,[11] take a few minutes and impede the imaging workflow. In a recent study by Yetisir et al.,[9] a 2D pTx pulse design approach for TSE sequences was introduced, involving 5 min of B_0 and B_1^+ field mapping followed by 10 s of pulse calculation for each slice. Unfortunately, experimental validation was limited to a phantom with smaller B_0 off-resonances compared to in vivo applications. Furthermore, this approach requires more than 5 min additional time for each imaging session, and a potential utilization of UP was not demonstrated. In contrast, our approach employs UP, eliminating the need for additional calibration calculations at the scanner, enabling seamless and straightforward utilization.

Compared to a B_1^+-shimmed multislice 2D T_2w TSE sequence, the slab-selective TSE demonstrates improved SNR and CJV with comparable CFR, albeit resulting in slightly blurrier images. Additionally, the B_1^+-shimming procedure necessitates 35 s of field mapping and calculation (of all slices), thereby extending the actual total acquisition time. Snyder et al.[43] previously highlighted that slab-selective TSE sequences experience SNR loss due to elimination of coherences through the 180° refocusing pulse and spoiler gradients. They have also indicated that B_1^+ inhomogeneities decrease SNR. However, this latter issue can be mitigated using pTx UP. For this reason, it was possible to achieve higher SNR with a slab-selective TSE sequence, as compared to conventional 2D TSE. Signal loss in the cerebellum due to B_1^+ field inhomogeneity was successfully mitigated with UPs. However, B_0 deviations still induce small signal dropouts in temporal and frontal lobes. Finally, the slab-selective TSE demonstates more robustness to motion artifacts, contributing to an clearer image overall in comparison to the 2D TSE sequence. This is attributed to the fact, that slab-selective TSE sequences allow higher turbo factors. Consequently, the smaller turbo factor of the 2D TSE sequence results in a higher volume TR and therefore increased susceptibility to motion artifacts.

For clinical applications 3D slab-selective FLAIR can be seamlessly implemented by adding a FLAIR T_2-prep module utilizing the 180° refocusing pulse and the phase coherent pulse of the refocusing train scaled to 90 deg as described in Reference 44.

5 | CONCLUSIONS

Our study demonstrates the feasibility of designing a compact set of three pulses to achieve phase coherent excitation in a slab-selective vFA TSE sequence with pTx at 7T. This concept is efficient to design subject tailored pulses as well as UP, the latter offering a user-friendly practical alternative for multislice TSE at 7T.

The simplicity of the approach makes it versatile: (1) UPs eliminate the need for a cumbersome calibration procedure at the scanner, particularly when employing GRAPE, (2) the initial nonselective optimization with k_T-points allows the user to select slab positions and orientations freely without the necessity of recomputing RF pulses, 3) compared to B_1^+-shimmed 2D TSE a substantial improvement in SNR and signal homogeneity could be achieved.

ACKNOWLEDGMENTS

This work received financial support from the European Union Horizon 2020 Research and Innovation program under grant agreement 885876 (AROMA).

ORCID

Daniel Lowen https://orcid.org/0000-0003-3709-9297
Eberhard D. Pracht https://orcid.org/0009-0008-4883-9709
Vincent Gras https://orcid.org/0000-0002-4997-2738
Franck Mauconduit https://orcid.org/0000-0002-0128-061X
Tony Stoecker https://orcid.org/0000-0002-8946-9141
Nicolas Boulant https://orcid.org/0000-0003-2144-2484

REFERENCES

1. Hennig J, Nauerth A, Friedburg H. RARE imaging: a fast imaging method for clinical MR. *Magn Reson Med*. 1986;3:823-833. doi:10.1002/mrm.1910030602
2. Mugler JP. Optimized three-dimensional fast-spin-echo MRI. *J Magn Reson Imaging*. 2014;39:745-767. doi:10.1002/jmri.24542
3. de Graaf WL, Zwanenburg JJM, Visser F, et al. Lesion detection at seven tesla in multiple sclerosis using magnetisation prepared 3D-FLAIR and 3D-DIR. *Eur Radiol*. 2012;22:221-231. doi:10.1007/s00330-011-2242-z
4. Bapst B, Amegnizin J, Vignaud A, et al. Post-contrast 3D T1-weighted TSE MR sequences (SPACE, CUBE, VISTA/BRAINVIEW, isoFSE, 3D MVOX): technical aspects and clinical applications. *J Neuroradiol*. 2020;47:358-368. doi:10.1016/j.neurad.2020.01.085
5. Šimić G, Kostović I, Winblad B, Bogdanović N. Volume and number of neurons of the human hippocampal formation in normal aging and Alzheimer's disease. *J Comp Neurol*. 1997;379:482-494. doi:10.1002/(SICI)1096-9861(19970324)379:4<482::AID-CNE2>3.0.CO;2-Z
6. de Lanerolle NC, Kim JH, Williamson A, et al. Erratum: a retrospective analysis of hippocampal pathology in human temporal lobe epilepsy: evidence for distinctive patient subcategories. *Epilepsia*. 2003;44:1131. doi:10.1046/j.1528-1157.2003.00448.x
7. Giuliano A, Donatelli G, Cosottini M, Tosetti M, Retico A, Fantacci M. Hippocampal subfields at ultra high field MRI: an overview of segmentation and measurement methods. *Hippocampus*. 2017;27:481-494. doi:10.1002/hipo.22717
8. Sbrizzi A, Hoogduin H, Hajnal JV, Van Den Berg CAT, Luijten PR, Malik SJ. Optimal control Design of Turbo Spin-echo Sequences with applications to parallel-transmit systems. *Magn Reson Med*. 2017;77:361-373. doi:10.1002/mrm.26084
9. Yetisir F, Poser BA, Grant PE, Adalsteinsson E, Wald LL, Guerin B. Parallel transmission 2D RARE imaging at 7T with transmit field inhomogeneity mitigation and local SAR control. *Magn Reson Imaging*. 2022;93:87-96. doi:10.1016/j.mri.2022.08.006
10. Eggenschwiler F, O'Brien KR, Gruetter R, Marques JP. Improving T 2 -weighted imaging at high field through the use of k T -points. *Magn Reson Med*. 2014;71:1478-1488. doi:10.1002/mrm.24805
11. Massire A, Vignaud A, Robert B, Le Bihan D, Boulant N, Amadon A. Parallel-transmission-enabled three-dimensional T2-weighted imaging of the human brain at 7 tesla. *Magn Reson Med*. 2015;73:2195-2203. doi:10.1002/mrm.25353
12. Berron D, Vieweg P, Hochkeppler A, et al. A protocol for manual segmentation of medial temporal lobe subregions in 7 tesla MRI. *Neuroimage Clin*. 2017;15:466-482. doi:10.1016/j.nicl.2017.05.022
13. Gras V, Vignaud A, Amadon A, Le Bihan D, Boulant N. Universal pulses: a new concept for calibration-free parallel transmission. *Magn Reson Med*. 2017;77:635-643. doi:10.1002/mrm.26148
14. Gras V, Pracht ED, Mauconduit F, Le Bihan D, Stöcker T, Boulant N. Robust nonadiabatic T2 preparation using Universal parallel-transmit kT-point pulses for 3D FLAIR imaging at 7 T. *Magn Reson Med*. 2019;81:3202-3208. doi:10.1002/mrm.27645
15. Van Damme L, Mauconduit F, Chambrion T, Boulant N, Gras V. Universal nonselective excitation and refocusing pulses with improved robustness to off-resonance for magnetic resonance imaging at 7 tesla with parallel transmission. *Magn Reson Med*. 2021;85:678-693. doi:10.1002/mrm.28441
16. Mugler JP, Bao S, Mulkern RV, et al. Optimized single-slab three-dimensional spin-echo MR imaging of the brain. *Radiology*. 2000;216:891-899. doi:10.1148/radiology.216.3.r00au46891
17. Mugler JP, Kiefer B, Brookeman JR. Three-dimensional T2-weighted imaging of the brain using very long spin-echo trains. *Joint Annual Meeting ISMRM-ESMRMB*. ISMRM; 2000.
18. Hennig J, Weigel M, Scheffler K. Calculation of flip angles for echo trains with predefined amplitudes with the extended phase graph (EPG)-algorithm: principles and applications to Hyperecho and TRAPS sequences. *Magn Reson Med*. 2004;51:68-80. doi:10.1002/mrm.10658
19. Pracht ED, Feiweier T, Ehses P, et al. SAR and scan-time optimized 3D whole-brain double inversion recovery imaging at 7T. *Magn Reson Med*. 2018;79:2620-2628. doi:10.1002/mrm.26913
20. Mitsouras D, Mulkern RV, Rybicki FJ. Strategies for inner volume 3D fast spin Echo magnetic resonance imaging using nonselective refocusing radio frequency pulses. *Med Phys*. 2006;33:173-186. doi:10.1118/1.2148331
21. Carr HY, Purcell EM. Effects of diffusion on free precession in nuclear magnetic resonance experiments. *Phys Rev*. 1954;94:630-638. doi:10.1103/PhysRev.94.630
22. Meiboom S, Gill D. Modified spin-echo method for measuring nuclear relaxation times. *Rev Sci Instrum*. 1958;29:688-691. doi:10.1063/1.1716296
23. Cloos MA, Boulant N, Luong M, et al. K T-points: short three-dimensional tailored RF pulses for flip-angle homogenization over an extended volume. *Magn Reson Med*. 2012;67:72-80. doi:10.1002/mrm.22978
24. Saïb G, Gras V, Mauconduit F, et al. Time-of-flight angiography at 7T using TONE double spokes with parallel transmission. *Magn Reson Imaging*. 2019;61:104-115. doi:10.1016/j.mri.2019.05.018
25. Gras V, Mauconduit F, Vignaud A, et al. Design of universal parallel-transmit refocusing k T -point pulses and application to 3D T 2-weighted imaging at 7T. *Magn Reson Med*. 2018;80:53-65. doi:10.1002/mrm.27001
26. Saïb G, Gras V, Mauconduit F, et al. kT-spokes combining kT-points with spokes to ease ramp pulse design for TOF slab

selection with parallel transmission at 7T. *Joint Annual Meeting ISMRM-ESMRMB*. ISMRM; 2018.
27. Jamil R, Mauconduit F, Gras V, Boulant N. General gradient delay correction method in bipolar multispoke RF pulses using trim blips. *Magn Reson Med*. 2021;85:1004-1012. doi:10.1002/mrm.28478
28. Setsompop K, Wald LL, Alagappan V, Gagoski BA, Adalsteinsson E. Magnitude least squares optimization for parallel radio frequency excitation design demonstrated at 7 tesla with eight channels. *Magn Reson Med*. 2008;59:908-915. doi:10.1002/mrm.21513
29. Khaneja N, Reiss T, Kehlet C, Schulte-Herbrüggen T, Glaser SJ. Optimal control of coupled spin dynamics: design of NMR pulse sequences by gradient ascent algorithms. *J Magn Reson*. 2005;172:296-305. doi:10.1016/j.jmr.2004.11.004
30. Pruessmann KP, Golay X, Stuber M, Scheidegger MB, Boesiger P. RF pulse concatenation for spatially selective inversion. *J Magn Reson*. 2000;146:58-65. doi:10.1006/jmre.2000.2107
31. Grissom W, Yip CY, Zhang Z, Stenger VA, Fessler JA, Noll DC. Spatial domain method for the design of RF pulses in multicoil parallel excitation. *Magn Reson Med*. 2006;56:620-629. doi:10.1002/mrm.20978
32. Gras V, Luong M, Amadon A, Boulant N. Joint design of kT-points trajectories and RF pulses under explicit SAR and power constraints in the large Flip angle regime. *J Magn Reson*. 2015;261:181-189. doi:10.1016/j.jmr.2015.10.017
33. Hoyos-Idrobo A, Weiss P, Massire A, Amadon A, Boulant N. On variant strategies to solve the magnitude least squares optimization problem in parallel transmission pulse design and under strict sar and power constraints. *IEEE Trans Med Imaging*. 2014;33:65. doi:10.1109/TMI.2013.22954
34. Kanayamay S, Kuhara S, Satoh K. In vivo rapid magnetic field measurement and shimming using single scan differential phase mapping. *Magn Reson Med*. 1996;36:637-642. doi:10.1002/mrm.1910360421
35. Yarnykh VL. Actual flip-angle imaging in the pulsed steady state: a method for rapid three-dimensional mapping of the transmitted radiofrequency field. *Magn Reson Med*. 2007;57:192-200. doi:10.1002/mrm.21120
36. Scheffler K. A pictorial description of steady-states in rapid magnetic resonance imaging. *Concepts Magn Reson*. 1999;11:291-304. doi:10.1002/(SICI)1099-0534(1999)11:5<291::AID-CMR2>3.0.CO;2-J
37. Weigel M. Extended phase graphs: dephasing, RF pulses, and echoes - pure and simple. *J Magn Reson Imaging*. 2015;41:266-295. doi:10.1002/jmri.24619
38. Dietrich O, Raya JG, Reeder SB, Reiser MF, Schoenberg SO. Measurement of signal-to-noise ratios in MR images: influence of multichannel coils, parallel imaging, and reconstruction filters. *J Magn Reson Imaging*. 2007;26:375–385. doi:10.1002/jmri.20969
39. Ganzetti M, Wenderoth N, Mantini D. Intensity inhomogeneity correction of structural MR images: a data-driven approach to define input algorithm parameters. *Frontiers. Neuroinformatics*. 2016;10:1-14. doi:10.3389/fninf.2016.00010
40. Cox RW. AFNI: software for analysis and visualization of functional magnetic resonance Neuroimages. *Comput Biomed Res*. 1996;29:162-173. doi:10.1006/cbmr.1996.0014
41. Cox RW, Hyde JS. Software tools for analysis and visualization of fMRI data. *NMR Biomed*. 1997;10:171-178. doi:10.1002/(SICI)1099-1492(199706/08)10:4/5<171::AID-NBM453>3.0.CO;2-L
42. Breuer FA, Blaimer M, Mueller MF, et al. Controlled aliasing in volumetric parallel imaging (2D CAIPIRINHA). *Magn Reson Med*. 2006;55:549–556. doi:10.1002/mrm.20787
43. Snyder J, Seres P, Wilman AH. SNR penalties from loss of stimulated echoes when using slab selective excitation in 3D fast spin Echo imaging with long Echo Trains. *NMR Biomed*. 2022;36:e4881. doi:10.1002/nbm.4881
44. Gras V, Mauconduit F, Vignaud A, et al. PASTeUR: package of anatomical sequences using parallel transmission UniveRsal kT-point pulses. *Joint Annual Meeting ISMRM-ESMRMB*. ISMRM; 2019.

SUPPORTING INFORMATION

Additional supporting information may be found in the online version of the article at the publisher's website.

Figure S1. Experimental validation of uniform slab selective excitation employing kT -spokes. A T1-weighted image (top left) depicts the position of two orthogonal slabs acquired with the same underlying kT -spokes pulse. The middle column displays the slab profile in sagittal view, while the right column shows the middle slice of each slab. The images were acquired utilizing a slab selective TSE with universal pulses.

Figure S2. Bloch simulation of universal pulses with ideal and real gradient shapes. Real gradient shapes were simulated by applying the measured gradient impulse response function (GIRF) to the ideal gradient trajectories. Additionally, the difference image (Diff) of both displayed slices is shown in the third column of each subject. Excitation (Exc) and both refocusing pulses (Ref 180 and Ref vFA) employed in the slab-selective TSE were simulated. Mean absolute flip angle differences across the entire head are provided below the flip angle and difference maps.

Figure S3. Comparison of the slab-selective TSE using various excitation pulses. Anatomical images are displayed on the left, with corresponding SNR maps shown on the right. Each column represents a different excitation pulse type: circularly polarized (CP) mode pulses, subject tailored pulses optimized with complex-least-squares (CLS), magnitude least-squares (MLS), or a combination of both (CLS+MLS) cost functions. At the left anatomical images are shown, and the corresponding SNR maps on the right hand side. Six slices of subject 1 are presented in six rows.

Figure S4. Comparison of the slab-selective TSE using various excitation pulses. Anatomical images are displayed on the left, with corresponding SNR maps shown on the right. Each column represents a different excitation pulse type: circularly polarized (CP) mode pulses, subject tailored pulses optimized with complex-least-squares (CLS), magnitude least-squares (MLS), or a combination of both (CLS+MLS) cost functions. At the left anatomical images

are shown, and the corresponding SNR maps on the right hand side. Six slices of subject 2 are presented in six rows.

Figure S5. Tailored vs. UP: Comparison of SNR maps, along with anatomical images for the slab-selective TSE sequence employing subject tailored pulses (ST) or universal pulses (UP). In both cases CLS+MLS excitation pulses were used. Six slices of two subjects are shown respectively.

Figure S6. SNR maps and anatomical images are compared for a 2D T2w TSE sequence with B+1-shimmed pulses and the slab selective TSE sequence employing universal pulses (UP) with high resolution protocols. Six slices of two subjects are shown respectively.

Figure S7. Average SNR across all voxels relative to the distance from the center of the field of view. Comparisons are made between acquisitions using slab-selective TSE with universal pulses (blue lines) and 2D T2w TSE with B+1-shimmed pulses (green lines) for two subjects.

How to cite this article: Lowen D, Pracht ED, Gras V, et al. Design of calibration-free RF pulses for T_2-weighted single-slab 3D turbo-spin-echo sequences at 7T utilizing parallel transmission. *Magn Reson Med*. 2024;92:2037-2050. doi: 10.1002/mrm.30212